Electronic Supplementary Information (ESI)

Excited-State Modulation via Alteration of the Heterocyclic Moiety in 9,9-Dimethylfluorene-Based Ir(III) Phosphorescent Dopants for Blue PhOLEDs

Bo-Sun Yun, So-Yoen Kim, Jin-Hyoung Kim, Sanghun Lee, Ho-Jin Son* and Sang Ook Kang*

Department of Advanced Materials Chemistry, Korea University, Sejong 30019, South Korea,

General Information

Spectroscopic Measurements. The steady-state absorption spectra were measured using a UV-Vis-NIR spectrophotometer (Agilent Technologies, Cary 5000). The steady-state emission spectra were measured using a fluorescence spectrophotometer (Varian, Cary Eclipse) equipped with high-performance R928 photomultiplier detector (high-performance R928) and CW Xenon lamp. For the measurement of phosphorescence spectrum at 77 K, the third harmonic (355 nm) pulse of a Q-switched Nd:YAG laser (Continuum, Surelite II; pulse width of 4.5 ns) was used as an excitation source.[1] The phosphorescence spectra were recorded using an ICCD detector (Andor, iStar) equipped with a monochromator (DongWoo Optron, Monora 500i). The temporal profiles were measured using a photomultiplier (Zolix Instruments Co., CR 131) and a digital oscilloscope (Tektronix, TDS-784D). Oxygen in the sample solutions was removed through the argon purging method.

Quantum Yield. Absolute PLQYs were obtained using a Quantaurus-QY measurement system (C11347-11, Hamamatsu Photonics), and all the samples were excited at 305 nm.

Electrochemical Analysis. The cyclic voltammetry experiments were performed using an electrochemical analyzer (Bioanalytical System Inc., BAS 100). The three-electrode cell system is comprised of a glassy carbon electrode as the working electrode, and platinum wire and $Ag/AgNO_3$ as a counter, and reference electrodes, respectively. Distilled and argon purged DMF and DCM were used as the solvent with 0.1 M tetrabutylammonium perchlorate electrolyte as the supporting electrolyte. The potential values were calibrated concerning the Fc/Fc^+ (Fc = Ferrocene) redox couple.

Theoretical Calculation. All the calculations were performed using the *Gaussian 09* program package.[2] The ground-state geometry was fully optimized using the density functional theory (DFT) level of the B3LYP (UB3LTYP for triplet calculation) method.[3,4] The 6-31G(d,p) and LANL2DZ basis sets were applied for non-metal atoms and iridium, respectively. The isodensity plots (contour = 0.03 a.u.) of the frontier orbitals were visualized by the GaussView 6 program. The TD-DFT calculation was performed to evaluate the vertical transition energies and oscillator strength for the singlet and triplet transitions.

Device Fabrication and Characterization. The OLED devices were fabricated on glass substrates, which were pre-coated with a 150 nm indium tin oxide (ITO) layer having a sheet resistance of 10 Ω/square. The ITO glass was precleaned sequentially with acetone (30 min), *N*-methyl-2-pyrrolidone (NMP) (30 min), deionized water, and isopropyl alcohol (IPA) (30 min), in an ultrasonic bath. The cleaned ITO glass was used immediately to fabricate the OLEDs. Before usage, the ITO substrates were treated with oxygen plasma. The organic and metal layers were deposited onto the ITO-coated glass substrate by thermal evaporation, and device fabrication was completed in a single cycle, without breaking the vacuum. The coated film was shadow masked to give four identical devices of area (2 mm × 2 mm). All the fabricated devices were encapsulated in N_2 glove box, before taking measurements. The current–voltage characteristics of OLEDs were analyzed using a source measurement unit (Keithley 2635B). The electroluminescence spectra, luminance, and CIE coordinates were measured by spectroradiometry (Konica Minolta CS-2000). Assuming Lambertian emission, the external quantum efficiency (EQE) was calculated from the luminance, current density, and electroluminescence spectrum.

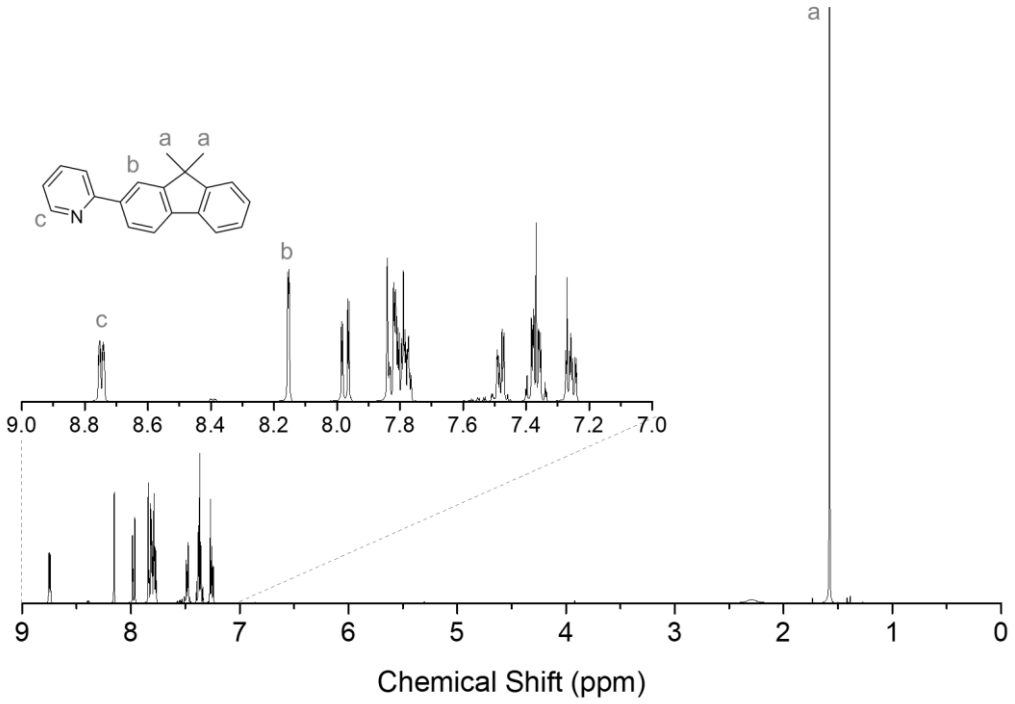

Fig. S1. [1]H-NMR spectra of 2-(9,9-dimethyl-9*H*-fluoren-2-yl)pyridine **(py)**.

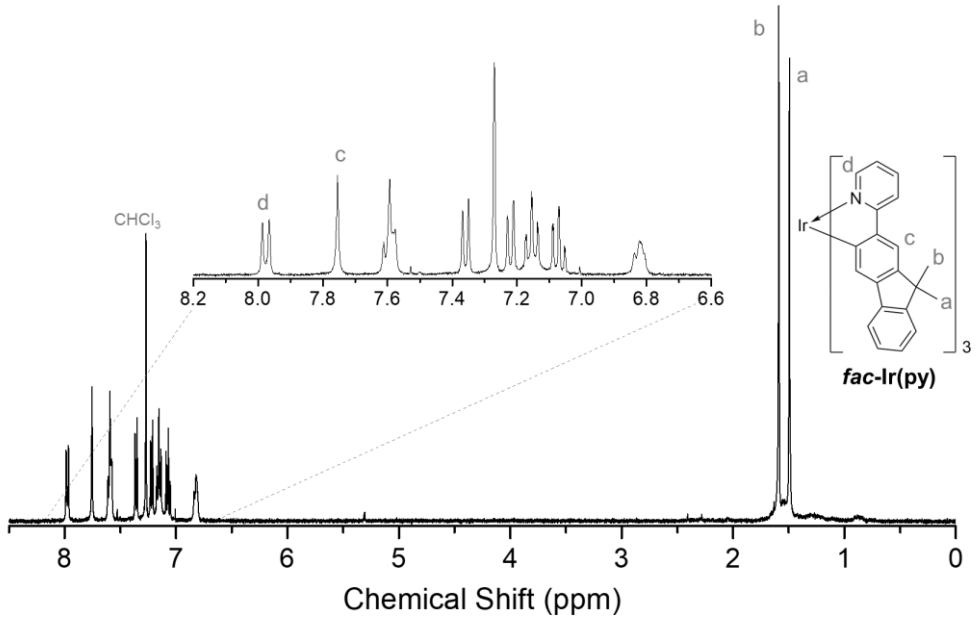

Fig. S2. [1]H-NMR spectra of ***fac*-Ir(py)**.

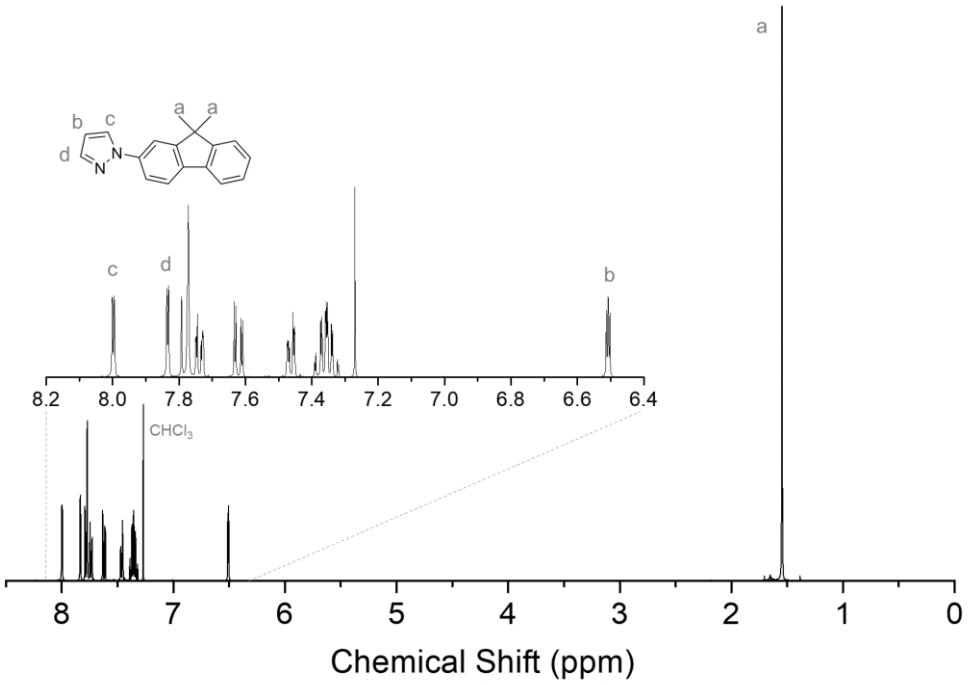

Fig. S3. [1]H-NMR spectra of 1-(9,9-dimethyl-9*H*-fluoren-2-yl)-1*H*-pyrazole **(pz)**.

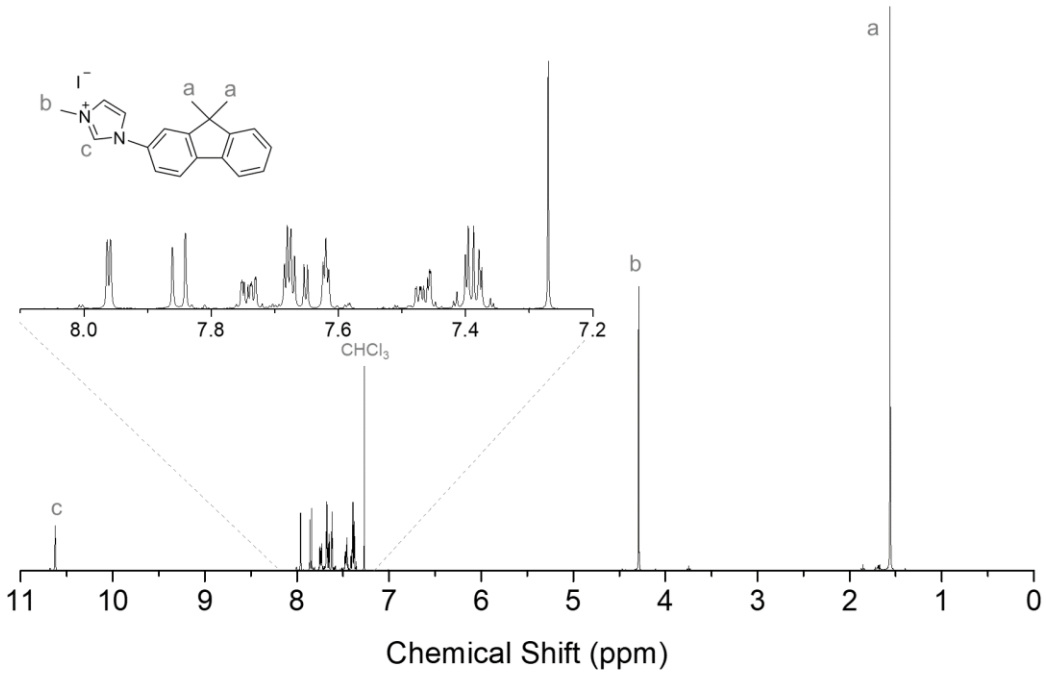

Fig. S4. [1]H-NMR spectra of 1-(9,9'-dimethyl-9*H*-fluoren-2-yl)-3-methyl-1*H*-imidazolium iodide **(im)**.

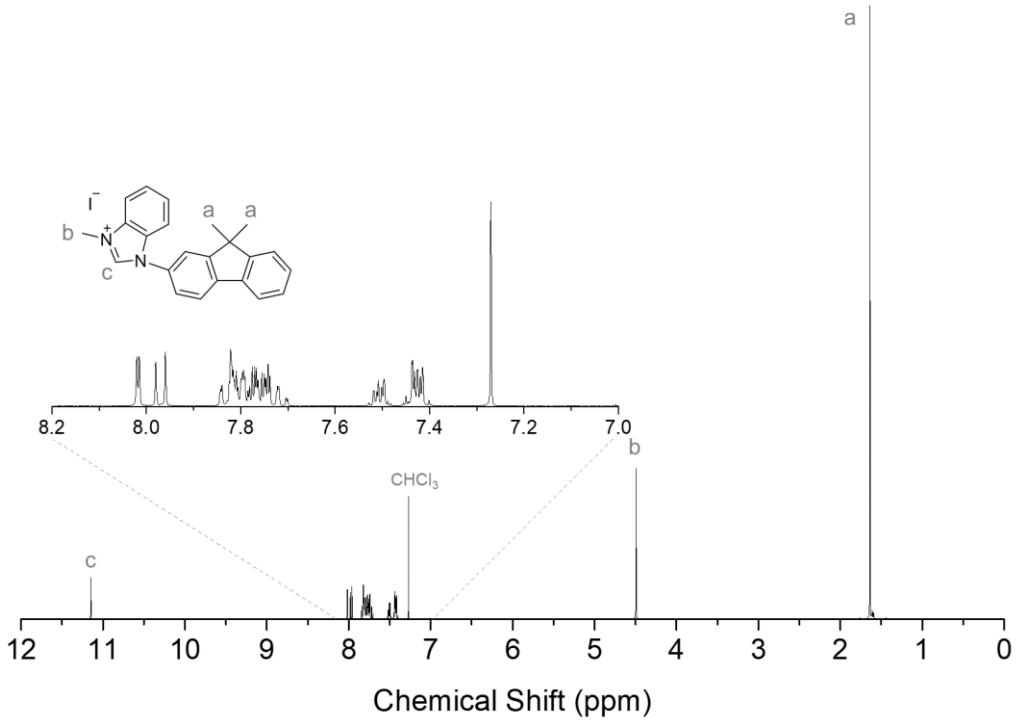

Fig. S5. [1]H-NMR spectra of 1-(9,9'-dimethyl-9*H*-fluoren-2-yl)-3-methyl-1*H*-benzimidazoli-um iodide **(bzim)**.

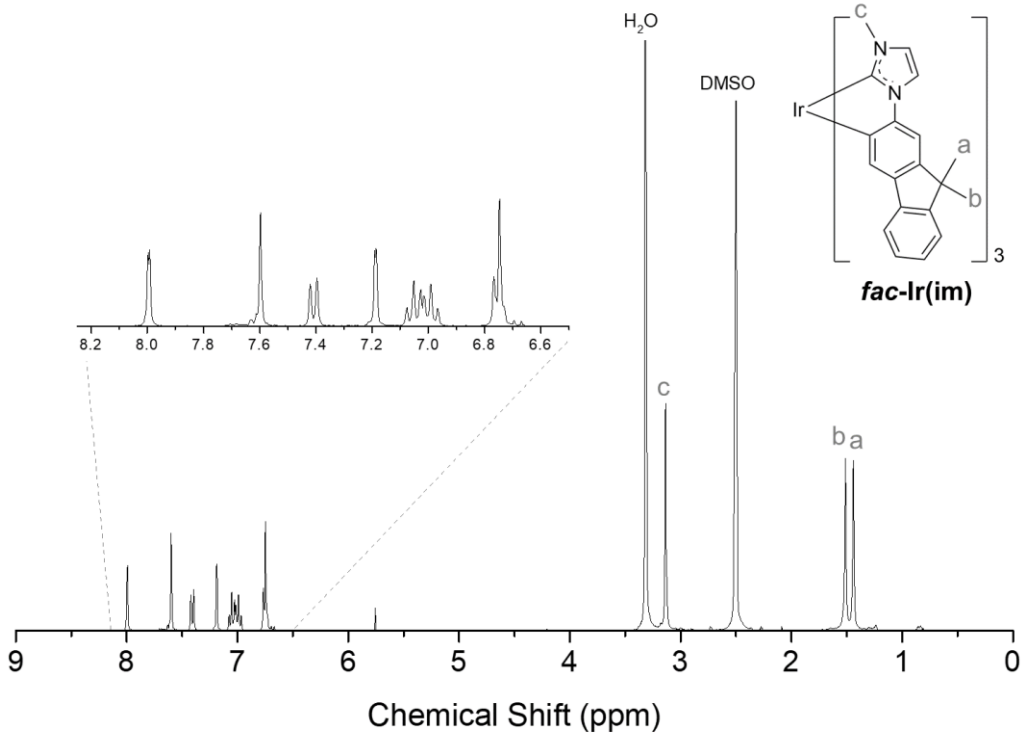

Fig. S6. [1]H-NMR spectra of ***fac*-Ir(im)**.

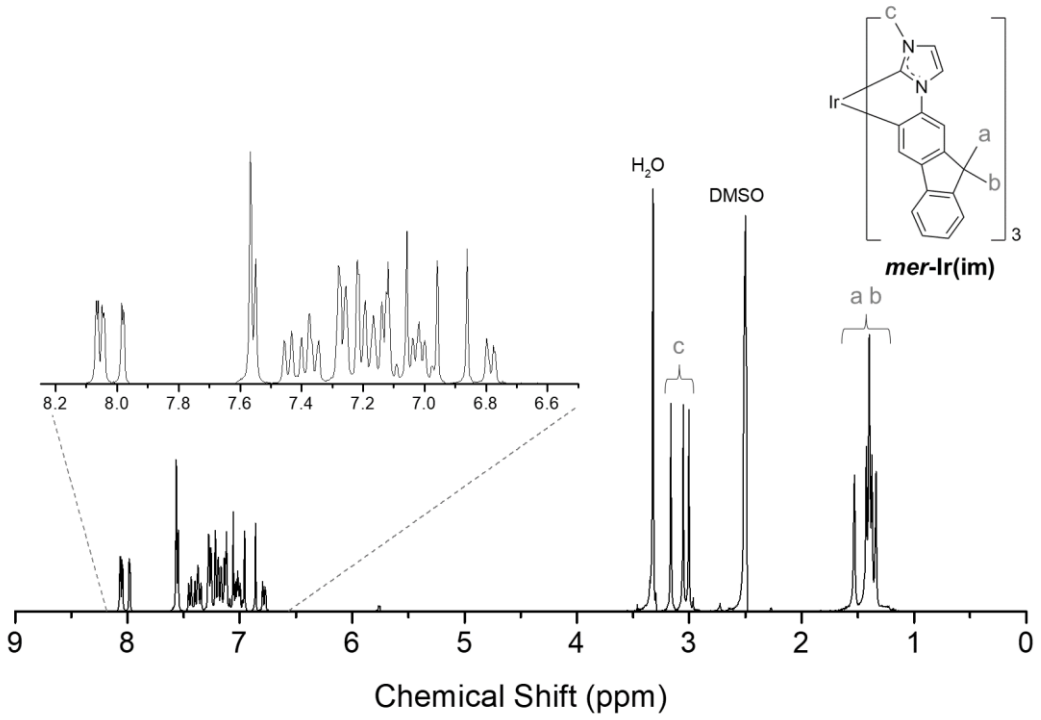

Fig. S7. [1]H-NMR spectra of ***mer*-Ir(im)**.

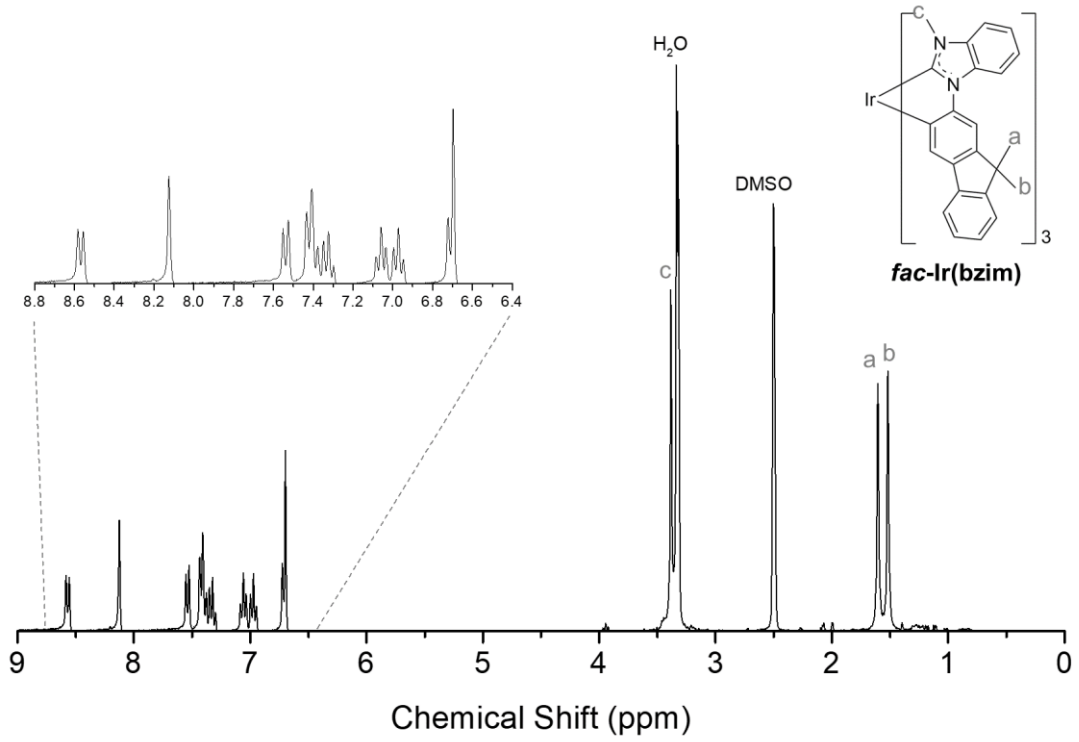

Fig. S8. [1]H-NMR spectra of ***fac*-Ir(bzim)**.

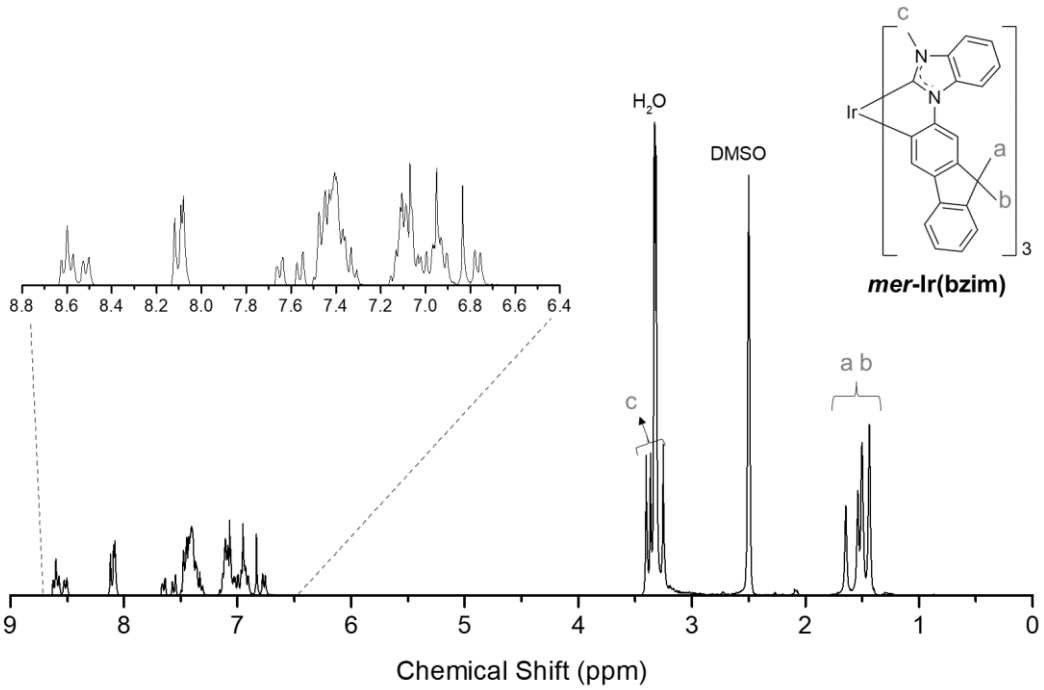

Fig. S9. ^{1}H-NMR spectra of ***mer*-Ir(bzim)**.

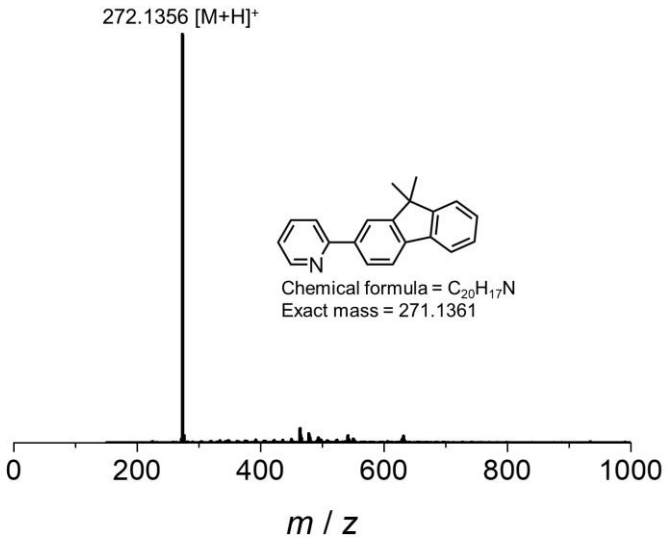

Fig. S10. ESI-Mass spectra of 2-(9,9-dimethyl-9*H*-fluoren-2-yl)pyridine **(py)**.

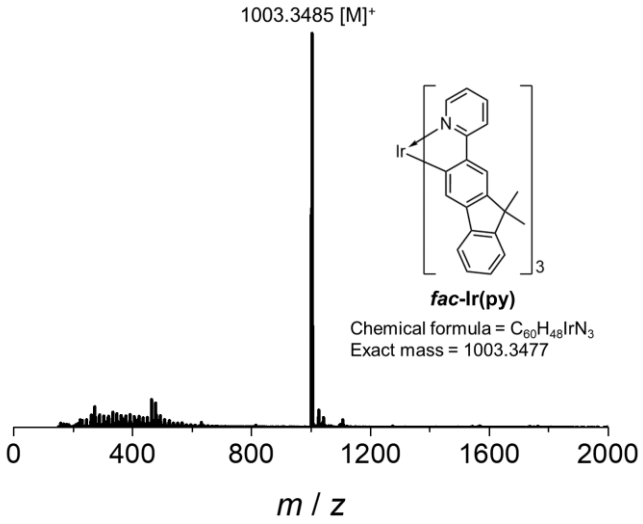

Fig. S11. ESI-Mass spectra of ***fac*-Ir(py)**.

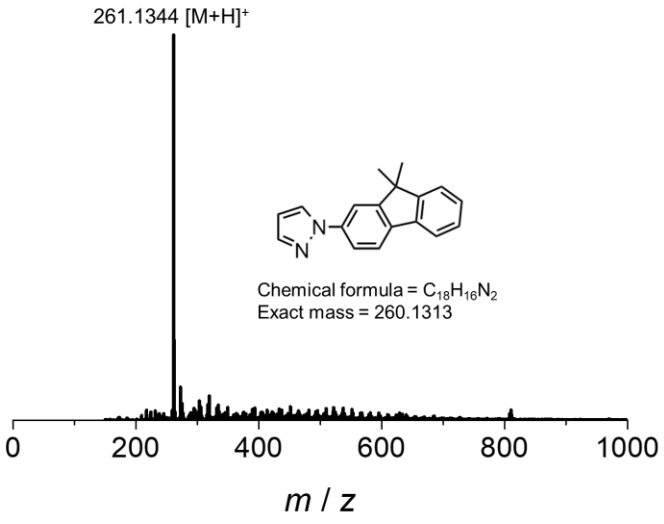

Fig. S12. ESI-Mass spectra of 1-(9,9-dimethyl-9*H*-fluoren-2-yl)-1*H*-pyrazole **(pz)**.

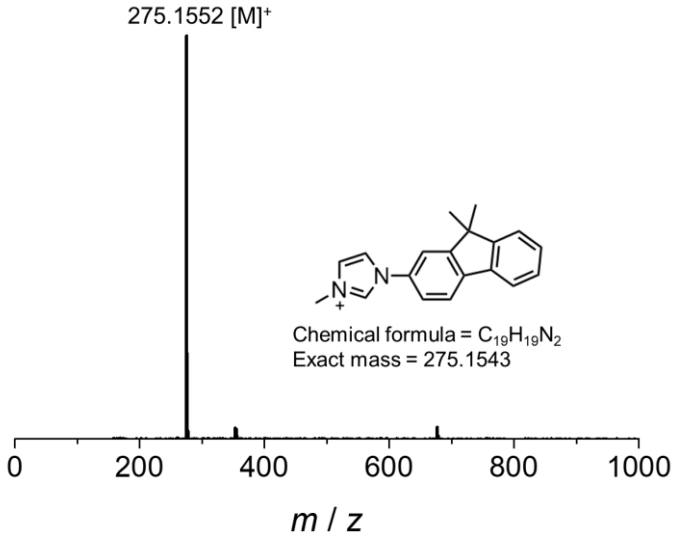

Fig. S13. ESI-Mass spectra of 1-(9,9'-dimethyl-9*H*-fluoren-2-yl)-3-methyl-1*H*-imidazolium iodide **(im)**.

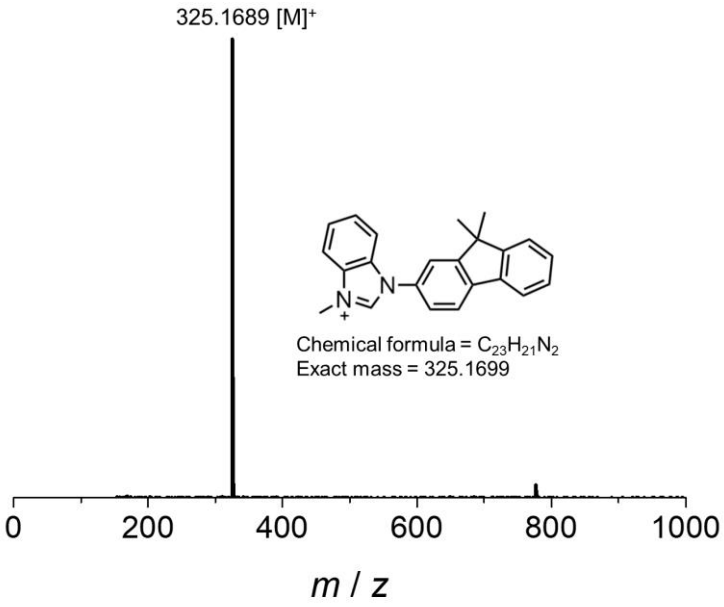

Fig. S14. ESI-Mass spectra of 1-(9,9'-dimethyl-9*H*-fluoren-2-yl)-3-methyl-1*H*-benzimidazoli-um iodide **(bzim)**.

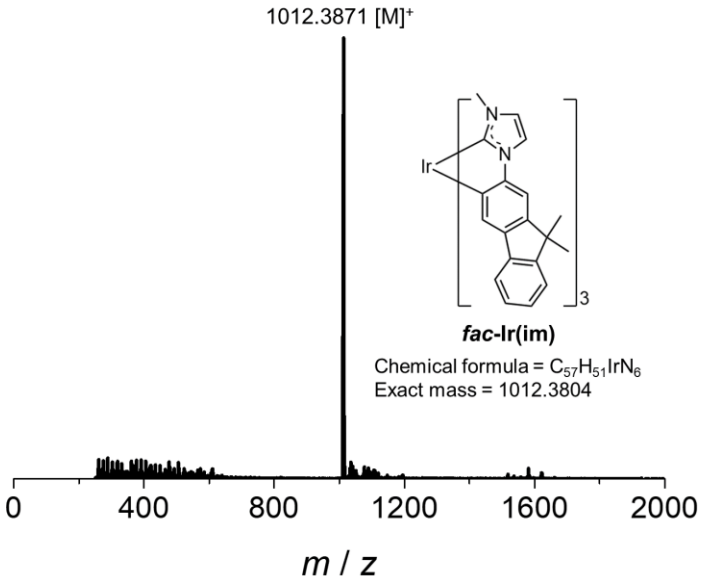

Fig. S15. ESI-Mass spectra of ***fac*-Ir(im)**.

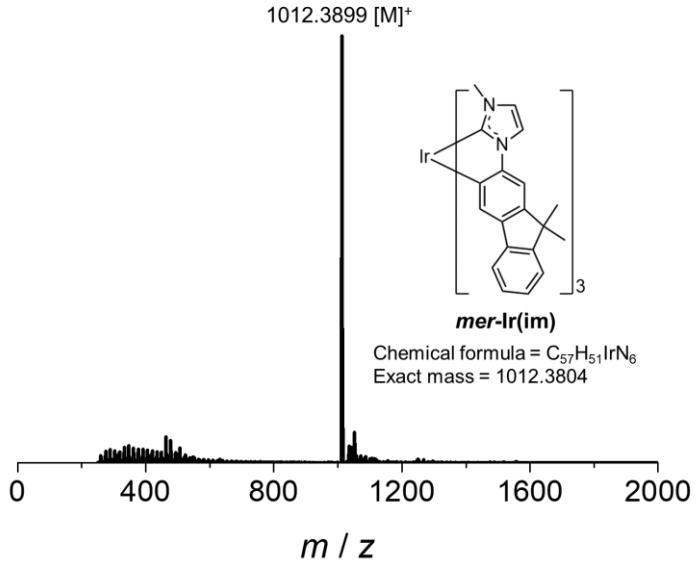

Fig. S16. ESI-Mass spectra of ***mer*-Ir(im)**.

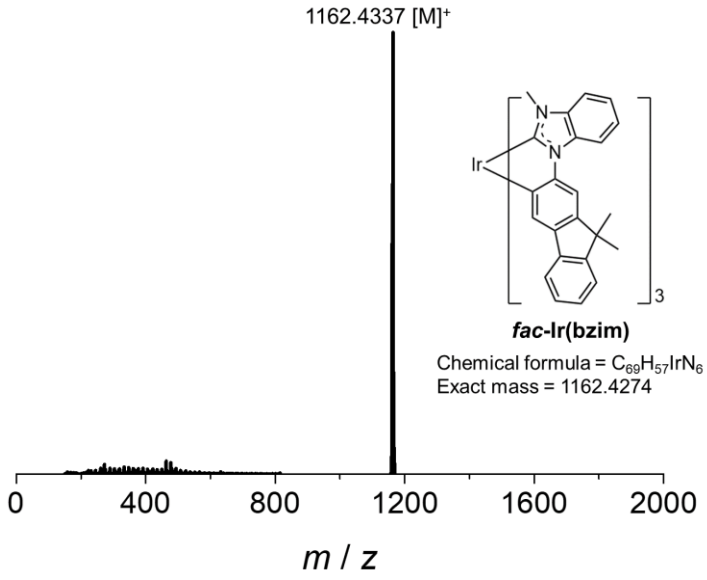

Fig. S17. ESI-Mass spectra of ***fac*-Ir(bzim)**.

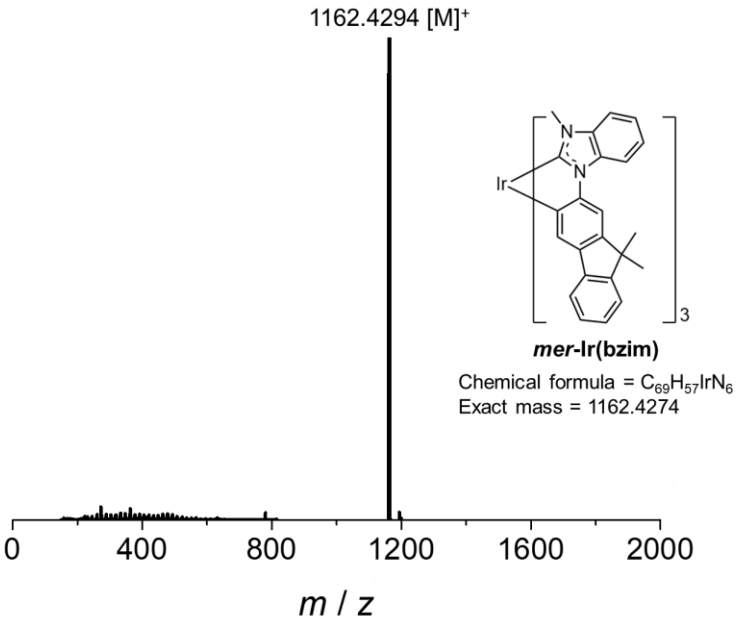

Fig. S18. ESI-Mass spectra of ***mer*-Ir(bzim)**.

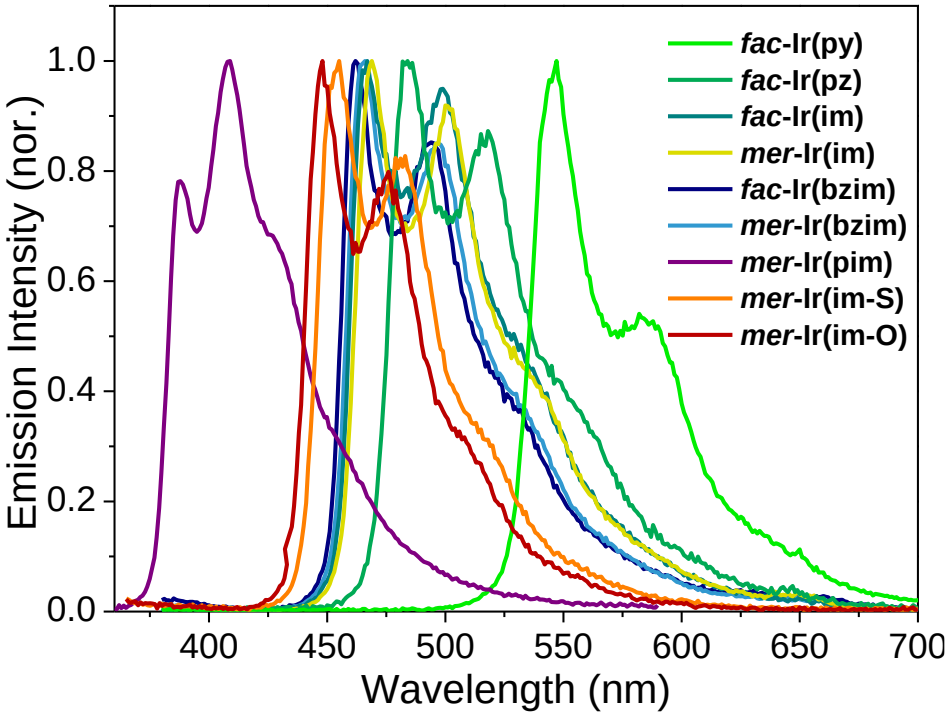

Fig. S19 Phosphorescence emission spectra of Ir(III) complexes in PMMA film

Table S1. Electrochemical properties of Ir(III) complexes

	$E_{1/2}^{ox}$ (V)	E^{red} (V)[a]	E_{HOMO} (eV)[b]	E_{LUMO} (eV)[c]	ΔE_g (eV)
***fac*-Ir(py)**	0.24 / 0.37	− 2.59	− 5.04	− 2.21	2.83
***fac*-Ir(pz)**	0.20 / 0.34	− 2.92	− 5.00	− 1.88	3.12
***fac*-Ir(im)**	0.15 / 0.23	− 3.25	− 4.95	− 1.55	3.40
***mer*-Ir(im)**	0.07 / 0.19	− 3.28	− 4.87	− 1.52	3.35
***fac*-Ir(bzim)**	0.38 / 0.50	− 3.11	− 5.18	− 1.69	3.49
***mer*-Ir(bzim)**	0.24 / 0.41	− 3.17	− 5.04	− 1.63	3.41
***mer*-Ir(pim)**	0.10 [d]	- [e]	− 4.90	− 1.68[f]	3.22[g]
***mer*-Ir(im-O)**	0.15 [d]	- [e]	− 4.95	− 2.17[f]	2.78[g]
***mer*-Ir(im-S)**	0.17 [d]	- [e]	− 4.97	− 2.20[f]	2.75[g]

[a] The E_{red} values were determined as the half-potential of the anodic peak and the cathodic peak in the case of ***fac*-Ir(py)**, and the onset-potential for the irreversible reduction peaks were determined to the other complexes. [b] The HOMO level was determined using the following equation: E_{HOMO} (eV) = $-e(E_{ox} + 4.8)$. [c] The LUMO level was determined using the following equation: E_{LUMO} (eV) = $-e(E_{red} + 4.8)$.[d] The $E_{1/2}^{ox}$ were detected in DCM solvent. [e] The reduction potential does not detected in DCM condition. [f] The E_{LUMO} was calculated using the following equation: E_{LUMO} (eV) = $e(E_{HOMO} + E_{0\text{-}0}^{opt})$. [g] The ΔE_g values were determined using a optical bandgap.

Table S2. Calculated transition energy and orbital transition analysis of Ir complexes

	State	λ_{cal}(E_{cal})	*f*	Orbital Contributions	Assignment
***fac*-Ir(py)**	T_1	518 nm (2.39 eV)	-	H→L (50%)	MLCT, ILCT
	S_1	449 nm (2.76 eV)	0.035	H→L (95%)	MLCT, ILCT
***fac*-Ir(pz)**	T_1	454 nm (2.73 eV)	-	H→L (41%)	MLCT, ILCT
	S_1	362 nm (3.43 eV)	0.067	H→L (92%)	MLCT, ILCT
***fac*-Ir(im)**	T_1	436 nm (2.84 eV)	-	H→L (31%)	MLCT, ILCT
	S_1	346 nm (3.58 eV)	0.080	H→L (95%)	MLCT, ILCT
***mer*-Ir(im)**	T_1	440 nm (2.82 eV)	-	H→L (16%), H→L+1 (10%)	MLCT, ILCT, LLCT
	S_1	359 nm (3.45 eV)	0.053	H→L (96%)	MLCT, ILCT, LLCT
***fac*-Ir(bzim)**	T_1	434 nm (2.86 eV)	-	H→L (10%)	MLCT, ILCT
	S_1	360 nm (3.44 eV)	0.042	H→L (91%)	MLCT, ILCT
***mer*-Ir(bzim)**	T_1	438 nm (2.83 eV)	-	H→L+1 (23%), H→L+3 (16%)	MLCT, ILCT, LLCT
	S_1	375 nm (3.31 eV)	0.012	H→L (91%)	MLCT, ILCT, LLCT
***mer*-Ir(pim)**	T_1	362 nm (3.42 eV)	-	H→L (10%), H→L+2 (27%)	MLCT, ILCT, LLCT
	S_1	319 nm (3.89 eV)	0.008	H→L (94%)	MLCT, ILCT, LLCT
***mer*-Ir(im-O)**	T_1	421 nm (2.94 eV)	-	H→L+1 (31%)	MLCT, ILCT, LLCT
	S_1	348 nm (3.56 eV)	0.059	H→L (93%)	MLCT, ILCT, LLCT
***mer*-Ir(im-S)**	T_1	425 nm (2.92 eV)	-	H→L (43%)	MLCT, ILCT, LLCT
	S_1	346 nm (3.58 eV)	0.024	H→L (86%)	MLCT, ILCT, LLCT

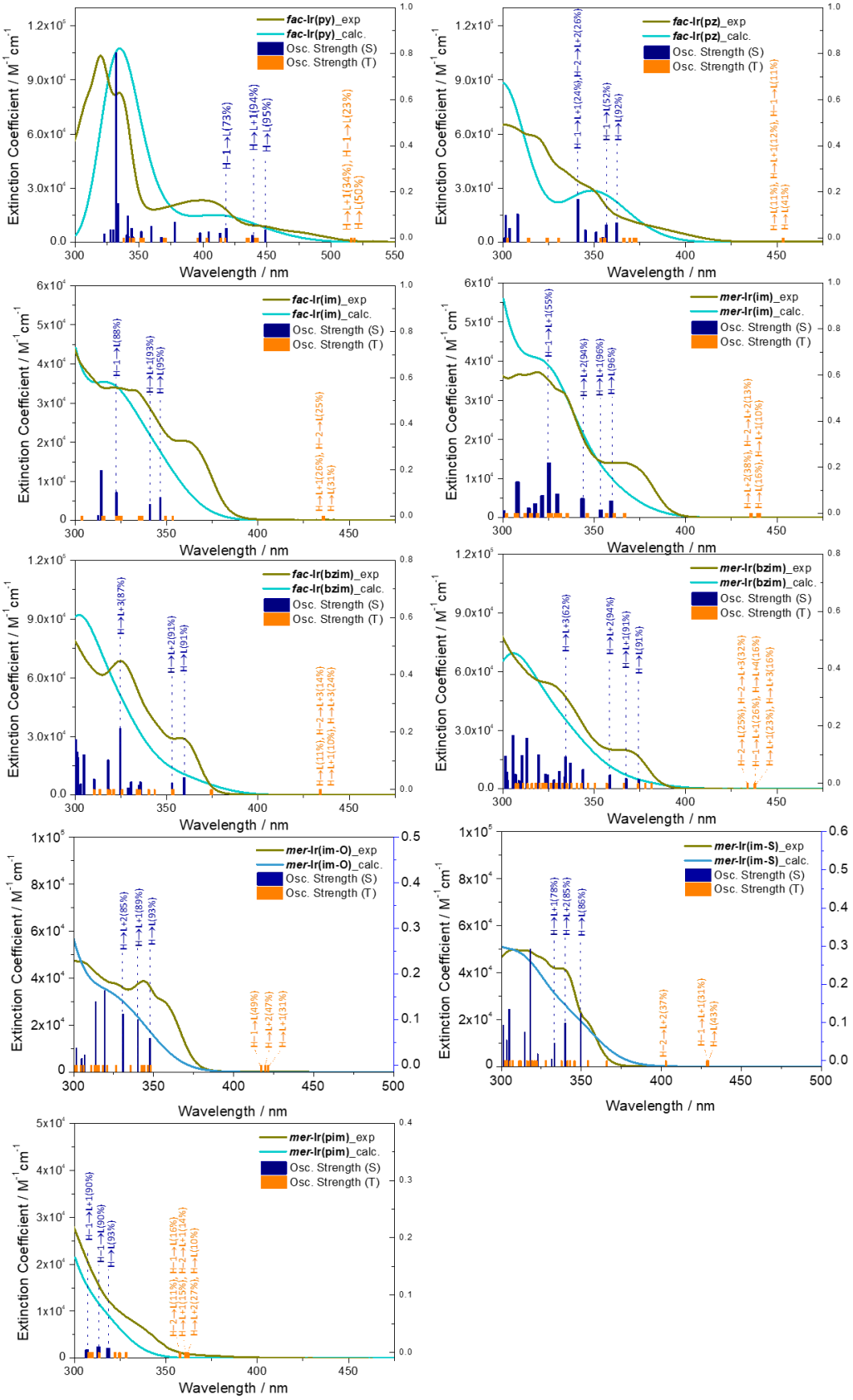

Fig. S20. Experimental spectra and predicted oscillator for Ir(III) complexes. Calculated oscillator strengths were obtained from Gaussian TD-DFT calculations.

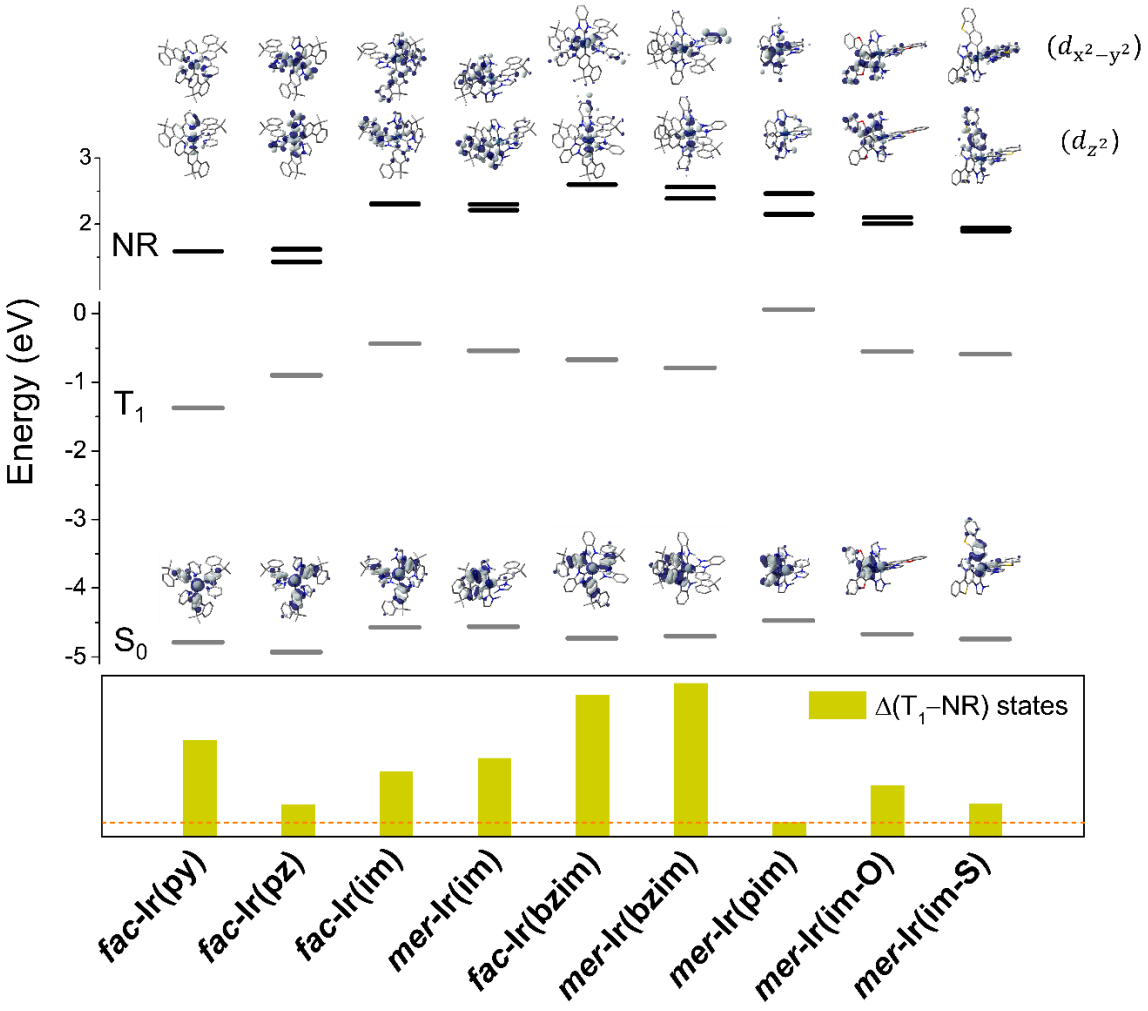

Fig. S21. Calculated S_0, T_1, and NR state energy levels and molecular orbital of S_0 and antibonding orbitals ($d_{z^2}/d_{x^2-y^2}$).

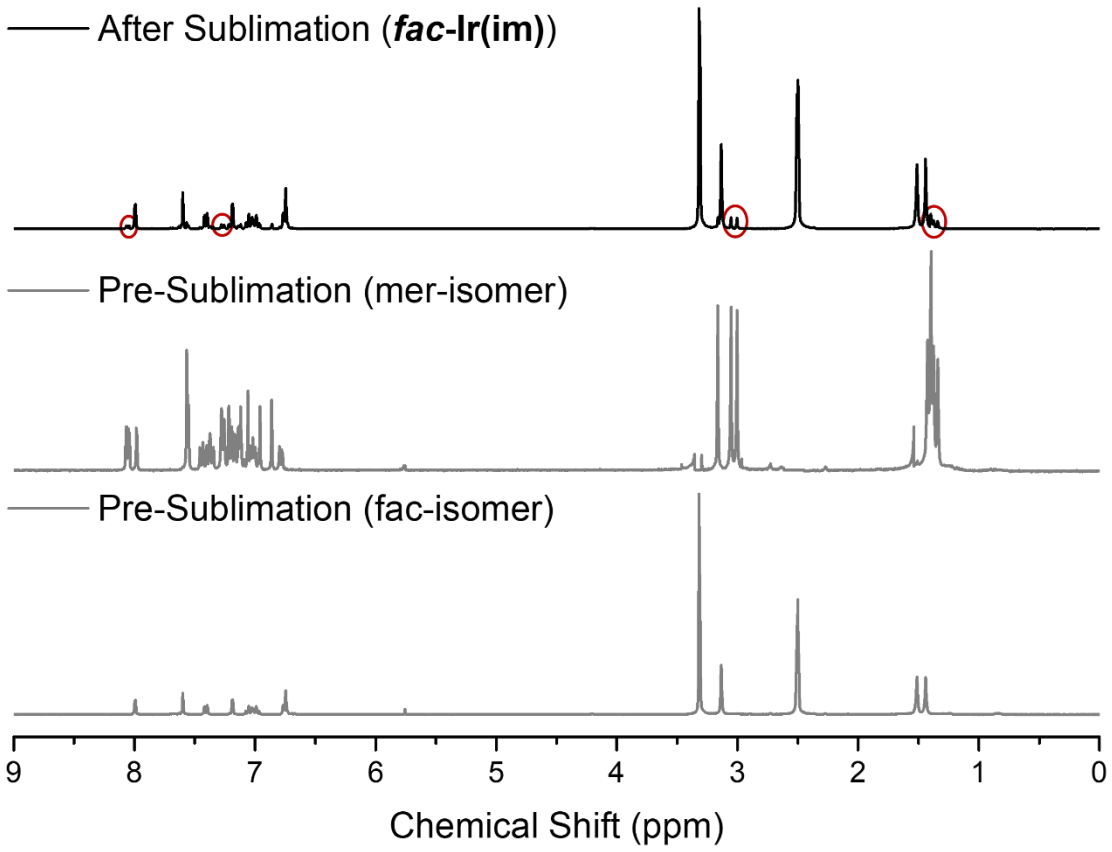

Fig. S22 ^{1}H-NMR spectra of ***fac*-Ir(im)** before and after sublimation.

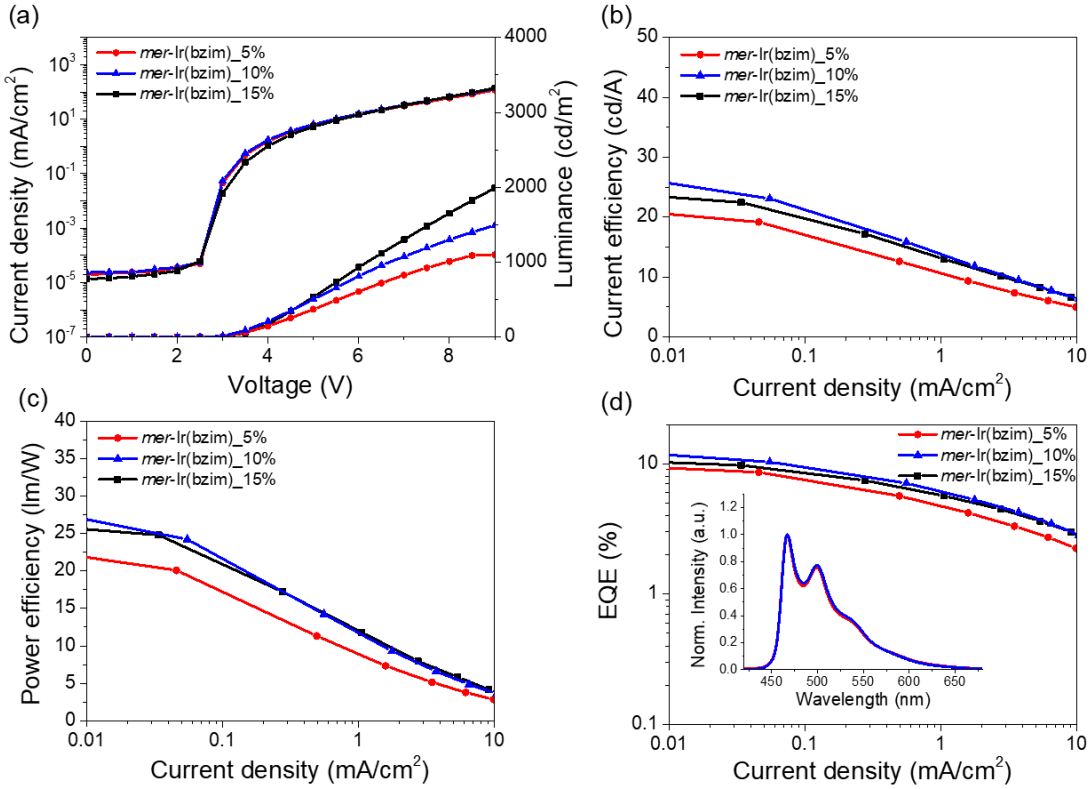

Fig. S23 Device performance for the **Devices III** with different ***mer*-Ir(bzim)** doping concentrations from 5% to 15%: (a) *J*-*V*-*L* characteristics, (b) current efficiency-current density curves, (c) power efficiency-current density curves, and (d) external quantum efficiency as a function of current density (inset: normalized EL spectra).

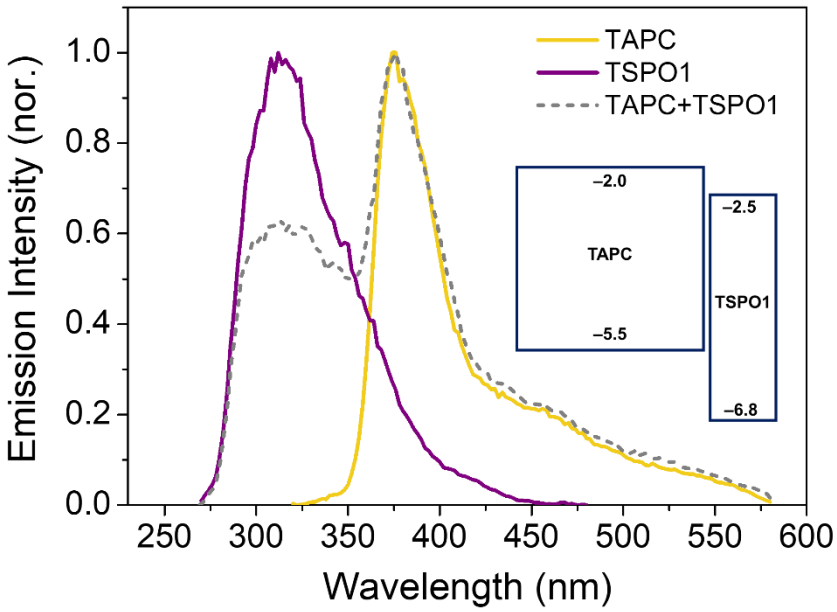

Fig. S24 Emission profiles of TAPC, TSPO1, and TAPC:TSPO1 films. From those experiments, we could not detect any additional emission peaks in the fabricated TSPO1:TAPC mixed film except for emission peaks from each single TSPO1 (λ_{em} = 315 nm) and TAPC film (λ_{em} = 375 nm). These results attest that an exciplex formation (from the LUMO of TSPO1 (2.5 eV) and the HOMO of TAPC (5.5 eV)) does not occur at the TSPO1/TAPC interface.